Research Square

Preprints are preliminary reports that have not undergone peer review.
They should not be considered conclusive, used to inform clinical practice,
or referenced by the media as validated information.

Ephaptic Aβ-to-C-Fiber Crosstalk Requires Multi-Fiber Spatial Summation: A Closed-Loop Core-Conductor Study with Nociceptor-Realistic Channel Kinetics

Mina Saied Attia

Mina.3024031@stemnewcairo.moe.edu.eg

New Cairo STEM School

Research Article

Keywords: ephaptic coupling, dynamic mechanical allodynia, core-conductor model, Nav1.8/Nav1.9 nociceptor kinetics, multi-fiber spatial summation, computational neuroscience

Posted Date: July 20th, 2026

DOI: https://doi.org/10.21203/rs.3.rs-10340019/v1

License: This work is licensed under a Creative Commons Attribution 4.0 International License.
Read Full License

Additional Declarations: No competing interests reported.

Abstract

Dynamic mechanical allodynia is often attributed to non-synaptic “ephaptic” cross-excitation between myelinated Aβ mechanoreceptive afferents and unmyelinated C-fiber nociceptors at sites of nerve compression or focal demyelination. We present a closed-loop, one-dimensional core-conductor model coupling a Chiu-Ritchie-Rogart-Stagg-Sweeney myelinated Aβ-fiber to a C-fiber through a shared extracellular cleft, tested in two phases. In Phase 1, using the field's standard classical Hodgkin-Huxley (HH) C-fiber kinetics, single-fiber-pair crosstalk fails under single-pulse stimulation (cleft widths 20 nm–5 μm), tonic sensitization, and temporal summation up to 800 Hz. In Phase 2, we replace the C-fiber's Na^+ conductance with literature-derived Nav1.8/Nav1.9 nociceptor kinetics and find crosstalk still fails, although the realistic channels now support a graded, stable sensitized state absent in classical HH, which instead transitions sharply into spontaneous firing or depolarization block. We then extend the model to a multi-fiber bundle in which several synchronously-active Aβ afferents share one extracellular compartment with a C-fiber. Using an artifact-detection protocol (timing, duration, geometry-independence) that proved necessary because the coupling scheme produces a reproducible spurious-firing signature past its stability ceiling, spatial summation across up to 25 verified-stable Aβ fibers produces a substantial, non-artifactual depolarization trend (≈ 8 mV) that no single-fiber-pair mechanism approached, without crossing threshold within the trustworthy range. These results indicate single-fiber-pair ephaptic crosstalk is an unlikely explanation for dynamic mechanical allodynia regardless of channel realism, while multi-fiber spatial summation is a plausible, partially-supported candidate mechanism whose confirmation requires the fully implicit numerical methods identified here as necessary future work.

1 Introduction

Dynamic mechanical allodynia (pain evoked by light, moving tactile stimuli such as brushing or clothing contact) is a hallmark of peripheral neuropathic pain conditions including painful diabetic neuropathy (Asmedi et al., 2018), post-herpetic neuralgia, and nerve entrapment syndromes such as trigeminal neuralgia (Rappaport & Devor, 1994). A long-standing biophysical hypothesis holds that, at sites of focal demyelination or mechanical nerve compression, the normally independent electrical activity of large myelinated Aβ mechanoreceptive afferents and small unmyelinated C-fiber nociceptors can become directly coupled through their shared, pathologically restricted extracellular space; a phenomenon first described by Arvanitaki (1942) and by Katz and Schmitt (1940) as “ephaptic” interaction. Experimental precedent for non-synaptic cross-excitation between afferent classes has since been reported directly in dorsal root ganglia (Amir & Devor, 2000; Devor & Wall, 1990) and in chronically damaged peripheral nerve (Rasminsky, 1980; Seltzer & Devor, 1979). Under this hypothesis, ordinary light touch, carried by Aβ fibers, could directly and non-synaptically trigger ectopic firing in a neighboring nociceptor, providing a purely peripheral account of allodynia that does not require central sensitization.

Prior computational treatments of ephaptic interaction in peripheral nerve have generally fallen into two categories: open-loop forward models, in which one fiber's field is imposed on a second fiber without

feedback (Lindén et al., 2014), and closed-loop models restricted to fibers of a single class, e.g., bundles of myelinated fibers or central white-matter tracts (Rossoni et al., 2003; Schmidt et al., 2021; Schmidt & Knösche, 2022). Dedicated simulation platforms and toolkits have extended these approaches to broader classes of ephaptic and extracellular-stimulation problems (Capllonch-Juan & Sepulveda, 2020; Marshall et al., 2025; Pelot et al., 2021; Shifman & Lewis, 2019). Ephaptic coupling has additionally been documented in central circuits such as cerebellar Purkinje cells (Han et al., 2018) and the olfactory bulb (Bokil et al., 2001), indicating the phenomenon is not restricted to peripheral nerve. To our knowledge, no published model has evaluated closed-loop, bidirectional ephaptic coupling between a myelinated Aβ fiber and an unmyelinated C-fiber using biophysically distinct, independently validated channel kinetics for each fiber type, under a systematically swept range of the pathological geometric parameter (extracellular cleft width) that is thought to govern coupling strength, nor has any such model tested whether spatial summation across a multi-fiber bundle can succeed where single-fiber-pair coupling fails.

This paper reports such a model, developed and evaluated in two phases. Phase 1 establishes a closed-loop core-conductor system coupling a CRRSS-kinetics myelinated Aβ-fiber and a classical Hodgkin-Huxley (HH) C-fiber (the field's standard baseline formulation) through a shared extracellular potential, and systematically tests whether direct Aβ→C ephaptic crosstalk can drive an ectopic C-fiber spike under single-pulse stimulation, tonic peripheral sensitization, and temporal summation from repetitive firing. Anticipating the principal biological objection to a classical-HH nociceptor model, Phase 2 replaces the C-fiber's Na^+ conductance with literature-derived Nav1.8/Nav1.9 nociceptor kinetics, re-validates the fiber and re-runs the Phase 1 experiment set, and then extends the model to a multi-fiber bundle geometry in which several simultaneously-active Aβ afferents converge on a shared extracellular compartment with one C-fiber, directly testing spatial summation as an alternative to single-fiber-pair crosstalk. We report that single-pair crosstalk fails consistently across both channel models, but that multi-fiber spatial summation (verified via a dedicated artifact-detection protocol described in Section 3) produces a substantial, non-artifactual trend toward threshold that no single-pair mechanism approached, making it the most promising direction identified for future work.

2 Methods

2.1 Coupled Core-Conductor Formulation

Two parallel, electrically independent axons of length L = 10 mm are embedded in a shared extracellular channel of longitudinal resistance per unit length r_e. For axon $k \in \{1, 2\}$ (Aβ, C), the transmembrane potential $v_{m,k} = u_{i,k} - u_e$ evolves according to the coupled cable equations

$$\partial v_{m,k}/\partial t = (1/C_{m,k}) \left[(d_k / 4\rho_i)(\partial^2 v_{m,k}/\partial z^2 + \partial^2 u_e/\partial z^2) - I_{ion,k} \right]$$

where d_k is fiber diameter, ρ_i is axoplasmic resistivity, and the shared extracellular potential u_e satisfies a regularized Poisson equation driven by the combined transmembrane ionic current of both fibers

(Section 2.3), following the classical extracellular field formulation of Clark and Plonsey (1968) and its cable-theoretic extension to endogenous-field coupling by Goldwyn and Rinzel (2016). In Section 2.5 this two-fiber system is generalized to n simultaneously-active Aβ fibers sharing the same extracellular compartment as one C-fiber. Figure 1 summarizes the resulting model architecture.

2.2 Membrane Kinetics

The Aβ-fiber (d = 10 μm) uses CRRSS kinetics (Chiu et al., 1979; Sweeney et al., 1987) in both phases of this study, with active Na^+ conductance and leak restricted to discrete nodes of Ranvier spaced 1 mm apart. Internodal compartments are assigned reduced membrane capacitance and leak conductance (250-fold lower than at nodes), reflecting the insulating effect of the myelin sheath; without this correction, saltatory propagation fails; an action potential initiated at one node does not reach the next, because internodal charge leaks away rather than passing passively forward. This requirement, while a standard feature of validated myelinated-fiber models, is easy to omit and was found empirically to be necessary during model validation (Section 3.1).

The C-fiber (d = 1 μm) is modeled in two variants across the two phases of this study. The Phase 1 (baseline) C-fiber uses classical Hodgkin-Huxley kinetics (Hodgkin & Huxley, 1952), continuously active along its length, parameterized to represent a generic cutaneous afferent; this is the field's standard formulation and the one on which essentially all prior closed-loop ephaptic models rely. The Phase 2 (nociceptor-realistic) C-fiber replaces this classical Na^+ conductance with Na*v*1.8/Na*v*1.9 kinetics, detailed in Section 2.5.

2.3 Extracellular Coupling and Regularization

The longitudinal extracellular resistance $r_e = \rho_e / A_{eff}$ is derived from the annular effective cross-sectional area of the extracellular cleft separating the fibers, parameterized by cleft width w_{cleft}. The governing equation for u_e under pure sealed-end (Neumann) boundary conditions is singular, defined only up to an additive constant. We therefore add a small regularization term κ, representing weak leakage of the restricted cleft's potential to the surrounding bulk tissue beyond the simulated segment:

$$\partial^2 u_e/\partial z^2 - \kappa \cdot u_e = r_e \cdot I_{total}(z)$$

κ was calibrated so that a single, physiologically realistic nodal Na^+ current produces an extracellular field on the order of a few millivolts, consistent with published estimates of ephaptic field magnitude in tightly restricted extracellular spaces (Goldwyn & Rinzel, 2016; Schlötter et al., 2023; Veeraraghavan et al., 2015). This calibration ($\kappa = 1\times10^9$ m^{-2}, field decay length ≈ 32 μm) was used for the two-fiber experiments in both phases (Sections 3.2 through 3.8). For the multi-fiber bundle (Section 2.6), the total source term scales with the number of simultaneously-active Aβ fibers; κ was accordingly re-verified, and where necessary strengthened, using the duration/timing/geometry-independence artifact-detection protocol described in Section 3.9, rather than assumed to transfer unchanged from the two-fiber calibration.

2.4 Numerical Scheme

The model is solved on a spatial grid of $\Delta z = 10$ μm ($N = 1000$ compartments). A naive fully-explicit (forward Euler) treatment of the axial diffusion term is numerically unstable at this spatial resolution; we therefore use an implicit–explicit (IMEX) splitting throughout: the linear axial diffusion term is integrated with backward Euler (solved as a tridiagonal system via LAPACK banded solvers), while the nonlinear ionic currents and the ephaptic coupling term are integrated explicitly from the previous time step's membrane state, and the shared extracellular potential is obtained by solving its regularized Poisson equation as a banded tridiagonal system at every time step. Phase 1 (classical HH C-fiber) uses $\Delta t = 5\times10^{-6}$ s, matching the temporal resolution needed for the CRRSS nodal Na^+ upstroke. Phase 2 (Na*v*1.8/1.9 C-fiber) requires a five-fold finer step, $\Delta t = 1\times10^{-6}$ s: the larger Na*v*1.8 conductance density needed for continuous propagation (Section 2.5) makes the explicit ionic-current update stiff at the coarser step, producing non-physiological voltage blow-up that we verified, by re-running at finer Δt, to be a discretization artifact rather than a genuine instability of the underlying dynamics.

This scheme is unconditionally stable with respect to axial diffusion but retains a stability ceiling on coupling strength (governed by κ and, in the multi-fiber case, by the number of simultaneously-active Aβ fibers) because the ephaptic feedback term itself is treated explicitly (Sections 3.6, 3.9).

2.5 Nav1.8/Nav1.9 Nociceptor Kinetics

The Phase 2 C-fiber's Na^+ current is modeled as the sum of a Na*v*1.8 component and a Na*v*1.9 component, each governed by first-order relaxation toward a voltage-dependent Boltzmann steady state, $dX/dt = (X_\infty(v) - X)/\tau_X$:

$I_{Na18} = \bar{g}_{18}\, m8^3\, h8\, (v - E_{Na}),\quad I_{Na19} = \bar{g}_{19}\, m9\, (v - E_{Na})$

$m8_\infty(v) = 1/[1 + \exp(-(v - V8m)/k8m)],\ V8m = -25\ mV,\ k8m = 6\ mV,\ \tau_{m8} = 1.5\ ms$

$h8_\infty(v) = 1/[1 + \exp((v - V8h)/k8h)],\ V8h = -30\ mV,\ k8h = 6\ mV,\ \tau_{h8} = 17\ ms$

$m9_\infty(v) = 1/[1 + \exp(-(v - V9m)/k9m)],\ V9m = -50\ mV,\ k9m = 5\ mV,\ \tau_{m9} = 10\ ms$

Na*v*1.8's depolarized, dominant-component activation/inactivation midpoints and its slow activation/inactivation time constants are drawn from voltage-clamp recordings of TTX-resistant current in small-diameter DRG neurons (Akopian et al., 1996; Klein et al., 2017); Na*v*1.9's markedly hyperpolarized activation midpoint and treatment as a persistent, non-inactivating current (single m-gate, no h-gate) follow its characterization as a subthreshold, near-non-inactivating conductance (Baker et al., 2003; Cummins et al., 1999). Voltage-independent time constants are a deliberate simplification for tractability; K^+ (classical delayed rectifier) and leak conductances are retained from the Phase 1 model unchanged, with leak reversal $E_{leak,2} = -55$ mV. Maximum conductance densities ($\bar{g}_{18} = 2000$ mS/cm², $\bar{g}_{19} = 0.2$ mS/cm²) were determined empirically: point-neuron rheobase testing first identified a stable, excitable regime at modest densities, but full-cable testing showed that Na*v*1.8's slow activation time

constant (τ_{m8} = 1.5 ms) gives continuous unmyelinated propagation a substantially lower safety factor than the classical HH Na^+ conductance's fast kinetics (τ_m ~ 0.1–0.5 ms) provide at the same density; $\bar{g}_{18}$ was increased, with K^+ density held at its classical value, until full-length continuous propagation was achieved and confirmed numerically stable at Δt = 1 μs (Section 3.7).

2.6 Multi-Fiber Bundle Formulation

To test spatial summation as an alternative to single-fiber-pair crosstalk, the two-fiber system of Section 2.1 is extended to n simultaneously-active, identical Aβ fibers sharing the same extracellular compartment as one Phase-2 C-fiber. Because all n Aβ fibers receive identical stimulation and are identically coupled to the same shared field, they evolve identically by symmetry; we therefore simulate a single representative Aβ cable and scale its contribution to the shared extracellular source term by n:

$$I_{total}(z) = n \cdot \pi d_1 I_{ion,1}(z) + \pi d_2 I_{ion,2}(z)$$

Each individual Aβ fiber's own membrane dynamics, and the ephaptic feedback it receives, are unaffected by n, consistent with this symmetric-copy assumption; only the field the ensemble collectively generates (and hence the drive felt by the C-fiber) scales with fiber count. This synchronous-firing configuration represents a receptive field in which a mechanical stimulus (e.g., a light touch or vibratory stroke) simultaneously recruits several Aβ mechanoreceptive afferents converging on a local Remak bundle; asynchronous or jittered multi-fiber recruitment is not tested here and is noted as a direction for future work (Section 5).

2.7 Simulation Protocols

Each experiment initiates a supra-threshold current pulse (100 nA, 0.2 ms, or a train thereof) at the first Aβ node of Ranvier (z = 0) and monitors the full spatiotemporal C-fiber membrane potential for any ectopic threshold crossing ($v_{m,2}$ > 0 mV) at locations away from the stimulation site and domain boundaries. Phase 1 (classical HH C-fiber, Sections 3.2–3.6) comprises: (1) a single-pulse sweep of cleft width from 20 nm to 5 μm; (2) tonic C-fiber sensitization, via a persistent depolarizing bias current and separately via a uniform shift of the HH gating kinetics (Section 2.8), each combined with single-pulse Aβ stimulation; (3) a temporal summation protocol delivering trains of 5–20 Aβ pulses at 50–800 Hz to a genuinely resting (unsensitized) C-fiber; and (4) a stronger-coupling stress test. Phase 2 (Na*v*1.8/1.9 C-fiber, Sections 3.7–3.9) re-validates the isolated fiber and repeats protocols (1)–(3) at reduced but representative sweep density, then extends to the multi-fiber bundle protocol of Section 2.6, sweeping both cleft width and Aβ fiber count n, with every candidate positive result subjected to the timing/duration/geometry-independence artifact-detection checks described in Section 3.6 and re-applied in Section 3.9.

2.8 Shifted-Kinetics Formulation for Sensitization (Section 3.4)

The Phase 1 sensitization test of Section 3.4 applies a uniform voltage offset ΔV_{shift} (mV) to the voltage argument of every classical HH rate function (both gates of the Na^+ channel and the K^+ activation gate) rather than to the Na^+ activation gate alone. For membrane potential v (mV), each rate is evaluated at v' = v + ΔV_{shift}:

α_m(v) = 0.1(v'+40) / [1 − exp(−(v'+40)/10)]

β_m(v) = 4·exp[−(v'+65)/18]

α_h(v) = 0.07·exp[−(v'+65)/20]

β_h(v) = 1 / [1 + exp(−(v'+35)/10)]

α_n(v) = 0.01(v'+55) / [1 − exp(−(v'+55)/10)]

β_n(v) = 0.125·exp[−(v'+65)/80], v' = v + ΔV_{shift}

with $\Delta V_{shift} > 0$ producing a leftward shift of the excitability curve. This uniform-shift formulation was adopted as a parsimonious first approximation of net inflammatory sensitization within the classical HH framework; Section 3.4 reports its behavior (spontaneous firing, not graded sensitization), motivating the Phase 2 Na*v*1.8/1.9 kinetics of Section 2.5, whose sensitization behavior is reported in Section 3.8.

3 Results

Sections 3.1 through 3.6 report Phase 1 (classical HH C-fiber) results, summarized in Table 1. Sections 3.7 through 3.9 report Phase 2 (Na*v*1.8/1.9 C-fiber) results, including the multi-fiber bundle experiment, summarized in Table 2.

3.1 Single-Fiber Validation and Positive Control

With myelin-corrected internodal parameters, the isolated Aβ-fiber conducted saltatorily through all ten simulated nodes of Ranvier with stable spike amplitude (~ 48 mV) and an estimated conduction velocity of 35.6 m/s, within the expected physiological range (30–60 m/s) for a 10 μm myelinated fiber. The isolated Phase 1 (classical HH) C-fiber conducted continuously at 0.57 m/s, within the expected range (0.5–1.0 m/s) for a cutaneous C-nociceptor. Both results were obtained with the coupling term disabled, confirming that each fiber's intrinsic kinetics behave as expected before closed-loop coupling was introduced.

These runs additionally serve as a positive control for every negative result reported below: they establish, using the identical spatial discretization and integration scheme used throughout the paper, that the Phase 1 C-fiber model is fully capable of generating and propagating a regenerative action potential when adequately driven (Fig. 2b). The Phase 2 C-fiber's independent positive control is reported in Section 3.7. The absence of ectopic firing in the coupled ephaptic experiments is therefore attributable

specifically to insufficient ephaptic drive relative to threshold, and not to a C-fiber implementation that is intrinsically unable to spike.

We additionally checked the sensitivity of the reported Aβ conduction velocity to spatial and temporal discretization. Halving Δz and Δt together (10 μm/5 μs → 5 μm/2.5 μs → 2.5 μm/1.25 μs) increased the estimated CV monotonically (35.6 → 42.6 → 49.6 m/s) rather than converging to a fixed value. This is not evidence of an unstable integration scheme (the IMEX solver itself remains stable, as verified in Section 2.4); rather, it reflects a structural property of representing each 1 mm internode's node of Ranvier as a single discrete compartment of width Δz. Because the model ties nodal membrane area to Δz rather than to the physiological node width (~ 1 μm), refining the grid inadvertently shrinks the simulated node's active membrane area, altering local excitability and hence CV. All results reported in this paper use the single, fixed discretization (Δz = 10 μm) described in Section 2.4 consistently across every experiment and every comparison between conditions, so the relative conclusions of this study (e.g., spike vs. no-spike, and the direction and rough scale of any depolarization trend) are unaffected; the absolute CV value, however, should be read as characteristic of this discretization rather than as a grid-independent physical prediction. Decoupling node width from Δz (e.g., by representing each node as a fixed physical patch spanning multiple fine compartments regardless of overall grid resolution) would be required to obtain a grid-independent CV, and is noted as a refinement for future work (Section 5).

3.2 Experiment 1: Single-Pulse Crosstalk (Phase 1)

No ectopic C-fiber spike was observed at any tested cleft width across the full range of 20 nm to 5 μm. The peak ephaptic perturbation of C-fiber membrane potential, measured away from the stimulation artifact, was approximately 2.8–4 mV; well below the ~ 10–15 mV depolarization required to reach threshold from rest. Consistent with the classical core-conductor picture of ephaptic interaction, the sign of the effect was spatially structured: at the location precisely aligned with a passing Aβ node, the induced perturbation was transiently hyperpolarizing, while depolarizing lobes of comparable magnitude occurred at flanking locations slightly offset in space and time from the source.

3.3 Sensitization via Persistent Depolarizing Bias (Phase 1)

A tonic depolarizing bias current was applied uniformly along the C-fiber to model peripheral sensitization by inflammatory mediators. At biases producing a steady-state resting depolarization to approximately − 55 to − 50 mV, combined with Aβ ephaptic input at cleft widths down to 50 nm, no threshold crossing occurred; the marginal ephaptic contribution above the elevated baseline remained small (~ 2–3 mV) regardless of cleft width. At larger biases sufficient to depolarize the resting potential further (toward − 30 mV or beyond), the C-fiber began firing spontaneously with no Aβ input whatsoever, indicating that these bias levels do not correspond to a genuinely stable sensitized resting state within classical HH kinetics but instead cross an intrinsic instability of the model.

3.4 Sensitization via Uniform HH Kinetics Shift (Phase 1)

As an alternative representation of inflammatory sensitization, we applied the uniform gating-kinetics shift defined in Section 2.8 to lower the effective firing threshold, without external current injection. Even a modest shift ($\Delta V_{shift} \geq 3$ mV) produced spontaneous, self-sustained repetitive firing with zero external input. This indicates that the classical HH parameter set exhibits a sharp transition between quiescence and spontaneous oscillation (consistent with the known Hopf-bifurcation structure of type II excitable membrane models) rather than a graded region in which the membrane is stably quiescent yet meaningfully closer to threshold. This structural property of classical HH channel kinetics, rather than an implementation error, directly motivated the Phase 2 nociceptor-realistic channel model (Section 2.5), whose sensitization behavior is reported in Section 3.8.

3.5 Temporal Summation (Phase 1)

To isolate genuine ephaptic summation from the confounds identified in Sections 3.3 and 3.4, trains of 5 to 20 Aβ pulses were delivered at frequencies from 50 to 800 Hz to a C-fiber held at its unmodified, independently-validated resting state (no tonic bias or kinetic shift). Long-duration control simulations (up to 300 ms) confirmed this baseline never fires spontaneously. Across the full combination of pulse train frequency, pulse count, and cleft width (50 nm to 1 μm), no ectopic spike occurred; maximal cumulative depolarization reached only 1–2 mV above rest, indicating that successive ephaptic pushes do not summate effectively at physiologically-calibrated coupling strength.

3.6 Stronger Coupling and Its Numerical Limits (Phase 1)

Motivated by literature reports of larger ephaptic field magnitudes in extremely tightly apposed membranes (e.g., cardiac intercalated-disc ephaptic coupling (Lin & Keener, 2010; Veeraraghavan et al., 2015)), we tested a substantially stronger coupling condition ($\kappa = 3\times10^{7}$ m^{-2}, decay length ≈ 183 μm), the strongest value for which a single-shot Poisson solve remained numerically stable. Under this condition, apparent ectopic spikes occurred, but with two features inconsistent with genuine ephaptic triggering: spike timing bore no relationship to the arrival of the Aβ action potential at the corresponding location (delays of up to several milliseconds rather than a sub-millisecond response), and, when the simulation window was extended, every tested cleft width (including a 1 μm cleft previously shown to be robustly stable under weaker coupling) eventually exhibited the same spurious firing. We conclude that this coupling regime exceeds the stability ceiling of the explicit-feedback numerical scheme described in Section 2.4, and that its apparent “results” reflect a numerical artifact rather than biophysics. This delayed-onset, geometry-independent spurious-firing signature (verified here for the first time) recurs whenever the scheme is pushed past its stability ceiling, and the same diagnostic protocol (timing relative to expected arrival; behavior under extended simulation duration; independence from the geometric parameter nominally being tested) is applied again in Section 3.9, where it proves essential.

Table 1
consolidates the outcome of every Phase 1 condition; no condition drawn from a physiologically-stable baseline produced genuine ephaptic threshold crossing.

Condition	Max Δv (mV)	Spike?
Single pulse, 20 nm–5 μm	~ 2.8–4	No
Mild bias + pulse	~ 2–3	No
Aggressive bias	n/a	Spontaneous*
Kinetics shift ≥ 3 mV	n/a	Spontaneous*
Summation, 50–800 Hz	~ 1–2	No
Strong coupling (κ = 3e7)	N/A	Artifact†

Table 1 Phase 1 (classical HH C-fiber): summary of experimental conditions and outcomes. *Fires independent of Aβ input, reflecting model instability rather than a genuine sensitized state. †Non-physiological, geometry-independent, delayed; attributed to explicit-scheme numerical instability (Sec. 3.6)

3.7 Nav1.8/Nav1.9 C-Fiber Validation (Phase 2)

Point-neuron rheobase testing located a stable resting state and a clear, regenerative excitation threshold for the Na*v*1.8/1.9 kinetics of Section 2.5 (rheobase between 0.5 and 1.0 nA for a 1 ms pulse; peak spike amplitude ~ 21–25 mV at near-rheobase current, consistent with the broader, smaller-amplitude action potentials typically reported for nociceptors relative to fast myelinated fibers). Full-cable testing, however, showed that classical-HH-scale Na^+ density (120–150 mS/cm²) does not support continuous propagation with Na*v*1.8's slow activation kinetics ($\tau m8$ = 1.5 ms): an action potential initiated at the stimulation site failed to recruit neighboring compartments and decayed within 2–3 mm. Increasing Na*v*1.8 density restored propagation, and full-length continuous conduction through all five tested positions (z = 1–9 mm) was achieved at $\bar{g}18$ = 2000 mS/cm² (Fig. 3a), confirmed numerically stable at Δt = 1 μs. The resulting conduction velocity, ≈ 0.36 m/s, is on the slow end of (but not inconsistent with) the physiological range reported for cutaneous C-nociceptors, and we report it as such rather than continuing to tune the model to match the Phase 1 classical-HH benchmark exactly. Long-duration (300 ms) simulation with no Aβ input confirmed the resting state is genuinely stable (identical results at 100 ms and 300 ms, no spontaneous firing), providing a positive control for Phase 2 directly analogous to that established for Phase 1 in Section 3.1.

3.8 Phase 2 Crosstalk Results (Nav1.8/Nav1.9 C-Fiber)

Single-pulse stimulation was re-run across the same cleft-width range as Phase 1 (20 nm–5 μm). No ectopic spike occurred at any cleft width; the peak ephaptic perturbation (~ 0.2–0.3 mV) was, if anything,

smaller than the Phase 1 classical-HH effect, consistent with the C-fiber's more depolarized resting potential and the Na*v*1.9 persistent current partially buffering small perturbations near rest.

Tonic sensitization via a persistent depolarizing bias current, re-tested with the Na*v*1.8/1.9 C-fiber, revealed a materially different (and more biologically plausible) failure structure than Phase 1. A genuinely graded, stable sensitized window exists: biases up to ~ 0.25 A/m² produced a stable elevated resting potential (up to ≈ − 56.8 mV) with no spontaneous activity, in contrast to classical HH's immediate transition to spontaneous firing. Above this window (bias ≳ 0.3 A/m²), however, the fiber does not fire repetitively; it instead settles into a sustained depolarized, silent state (depolarization block, driven by near-complete Na*v*1.8 inactivation); a different, but still non-physiological, failure mode. Combining ephaptic input with sensitization at the edge of the genuinely stable window (bias 0.2–0.28 A/m², cleft widths down to 20 nm) still produced no threshold crossing; the marginal ephaptic contribution remained under 1 mV, far short of the several-millivolt gap remaining to threshold even at the most favorable bias tested.

Temporal summation, re-tested at reduced but representative sweep density (200–400 Hz, 5–10 pulses, cleft widths 20–200 nm, unsensitized C-fiber), likewise produced no ectopic spike, consistent with both Phase 1 and the single-pulse Phase 2 result above.

In summary, replacing classical HH kinetics with literature-derived Na*v*1.8/1.9 nociceptor kinetics changes the qualitative behavior of sensitization (producing a genuine, if narrow, graded stable window rather than classical HH's sharp bifurcation) but does not change the bottom-line conclusion: single-fiber-pair ephaptic crosstalk remains insufficient under any tested combination of stimulation, sensitization, or summation.

3.9 Multi-Fiber Bundle Spatial Summation (Phase 2)

Motivated by the consistent failure of single-fiber-pair mechanisms in both phases, we tested the multi-fiber bundle formulation of Section 2.6: n synchronously-firing Aβ fibers sharing one extracellular compartment with an unsensitized Na*v*1.8/1.9 C-fiber. An initial sweep at the Section 2.3 two-fiber calibration ($\kappa = 1\times10^{9}$ m^{-2}) produced an apparent ectopic spike at n = 5 (cleft 200 nm). Applying the artifact-detection protocol established in Section 3.6 immediately identified this as spurious: the threshold crossing occurred 0.40 ms after stimulation at a location the Aβ wave reached at 0.08 ms (a 0.32 ms unexplained delay) and extending the simulation window showed that nominally “stable” nearby conditions (n = 3 and n = 5 at a narrower cleft) also eventually fired spuriously given more time, while genuine two-fiber-equivalent conditions (n = 1) did not. This behavior is the same delayed-onset, duration-dependent, non-monotonic-in-geometry signature documented in Section 3.6, now triggered by total Aβ source current scaling with n rather than by κ directly.

We therefore re-calibrated κ specifically for the multi-fiber source magnitude, verifying at each step (via extended-duration simulation (up to 18 ms, several-fold longer than the 2–3 ms window in which genuine ephaptic responses complete) and timing checks against expected Aβ arrival) that reported outcomes

are genuine rather than artifactual. At $\kappa = 5\times10^{9}$ m^{-2}, n = 1–8 remained stable under extended duration; at $\kappa = 2\times10^{10}$ m^{-2}, stability under extended duration (confirmed to 18 ms) extended to n = 25. Beyond this (n = 40 tested at $\kappa = 2\times10^{10}$ m^{-2}) the same delayed-onset artifact reappeared (first crossing at 3.31 ms against an expected arrival of 0.17 ms), and was excluded from the reported result.

Within the numerically verified-stable range (n = 1 to 25), spatial summation produced a substantial, monotonic, non-artifactual depolarization trend: peak C-fiber membrane potential shifted from − 55.0 mV (n = 1, indistinguishable from the two-fiber result of Section 3.8) to − 47.5 mV (n = 25); an ≈ 8 mV effect, roughly an order of magnitude larger than any single-fiber-pair mechanism tested in either phase, and confirmed stable under an 18 ms simulation window (Fig. 3b). This trend did not cross threshold within the verified-stable range, and we explicitly do not claim that it would with additional fibers; extending the trend beyond n = 25 requires a numerical scheme not limited by the explicit-coupling stability ceiling identified in Sections 3.6 and 3.9 (see Section 5).

Table 2
Phase 2 (Nav1.8/Nav1.9 C-fiber): summary of experimental conditions and outcomes. *Sustained depolarized, silent state (near-complete Nav1.8 inactivation), not repetitive firing. †Delayed-onset, duration-dependent; excluded as non-physiological per the Sections 3.6/3.9 artifact-detection protocol

Condition (Phase 2)	**Max Δv (mV)**	**Spike?**
Single pulse, 20 nm–5 μm	~ 0.2–0.3	No
Graded bias (≤ 0.25 A/m²)	stable, subthresh.	No
Bias + pulse (edge of window)	< 1	No
Aggressive bias (≳ 0.3 A/m²)	n/a	Depol. block*
Summation, 200–400 Hz	~ 1	No
Multi-fiber, n = 1–25 (verified)	≈ 8 (trend)	No (trending)
Multi-fiber, n = 40 (κ = 2e10)	N/A	Artifact†

4 Discussion

Across both phases of this study (classical HH and literature-derived Na*v*1.8/1.9 C-fiber kinetics) and across single-pulse stimulation, tonic sensitization, and high-frequency temporal summation, direct Aβ-to-C ephaptic coupling between a single fiber pair never drives an ectopic nociceptor spike at physiologically-calibrated coupling strength. This convergence across two biophysically distinct channel models is, we argue, stronger evidence against single-fiber-pair crosstalk as a stand-alone allodynia mechanism than either phase would provide alone: it rules out the specific objection that a classical-HH nociceptor model is simply the wrong biology, since replacing it with realistic Na*v*1.8/1.9 kinetics (which do materially change how the model fails (a genuine, if narrow, graded sensitized window rather than an immediate bifurcation into spontaneous firing)) does not change the outcome.

What does change the outcome, at least partially, is abandoning the single-fiber-pair assumption altogether. The multi-fiber bundle result of Section 3.9 is the first mechanism tested in this study, across either phase, to produce a substantial, non-artifactual trend toward threshold (an order of magnitude larger than any single-pair effect) and it is directly compatible with the anatomy motivating the ephaptic hypothesis in the first place: a Remak bundle or compressed nerve segment does not contain one Aβ fiber and one C-fiber in isolation, but many afferents of both types sharing a genuinely restricted extracellular space. A mechanical stimulus recruiting several Aβ mechanoreceptors simultaneously (as ordinary light touch or a brushing stimulus naturally would) is precisely the scenario the multi-fiber protocol models. This is also consistent with the earliest experimental reports of cross-excitation in dorsal root ganglia, which document functional coupling between populations of afferents rather than isolated fiber pairs (Amir & Devor, 2000; Devor & Wall, 1990).

This finding must, however, be reported with the same caution applied throughout this study to any candidate positive result. We could not extend the verified-stable range past n = 25 fibers without encountering the same explicit-coupling numerical artifact documented in Section 3.6, and we make no claim about whether the trend observed here would continue, saturate, or cross threshold at larger, more anatomically realistic bundle sizes. The honest conclusion is that multi-fiber spatial summation is a mechanistically plausible and partially-supported candidate mechanism for ephaptic contributions to dynamic mechanical allodynia (the most promising of everything tested in this study) whose confirmation or refutation requires numerical methods not limited by the stability ceiling identified here.

4.1 Limitations

This study uses a one-dimensional core-conductor approximation of a fully three-dimensional, tortuous extracellular geometry and a purely ohmic extracellular medium. As established in Section 3.1, the reported Aβ conduction velocity is discretization-dependent because nodal membrane area is tied to Δz rather than fixed at the physiological node width; all comparisons in this study use a single, consistent discretization, but the absolute CV should not be over-interpreted as a grid-independent physical prediction. The multi-fiber bundle (Section 2.6) assumes identical, perfectly synchronous Aβ fibers by symmetry; asynchronous recruitment, fiber-to-fiber heterogeneity, and summation among multiple C-fibers (rather than convergence onto one) are not tested. The extracellular regularization parameter κ, while calibrated to produce physiologically plausible field magnitudes for a single active node and re-verified for the multi-fiber source magnitude, is not derived from first-principles bundle histology. Most importantly, the explicit treatment of the ephaptic feedback term imposes a hard numerical ceiling ($n \leq 25$ fibers in this study) beyond which candidate results cannot currently be distinguished from artifact; this ceiling, not any biophysical saturation, is what bounds our multi-fiber conclusion.

The 1D approximation in particular assumes a uniform, annular extracellular cleft along the full fiber length. Real compressed or demyelinated nerve segments instead present highly tortuous, non-uniform 3D extracellular spaces, in which locally tight pockets of apposition can produce field concentrations that a longitudinally-averaged 1D cable equation is structurally unable to represent. Fully coupled 3D

finite-element Extracellular–Membrane–Intracellular (EMI) formulations, recently applied to ephaptic coupling and extracellular stimulation in central neurons (Jæger et al., 2021; Jæger & Tveito, 2026), provide a template for such a model; applying this approach to the true extracellular geometry of a compressed or demyelinated peripheral nerve bundle could both reveal localized field hotspots that the 1D approximation averages out and, being naturally suited to multi-fiber geometries, remove the explicit-coupling ceiling that bounds the present multi-fiber result.

5 Future Work

Five extensions follow directly from the results and limitations above. (1) A fully implicit joint solver for the coupled cable, multi-fiber source, and extracellular Poisson systems is now concretely motivated, not merely plausible: it is the specific requirement for testing whether the multi-fiber trend of Section 3.9 continues past n = 25 and crosses threshold at anatomically realistic bundle sizes, and would remove the explicit-coupling stability ceiling documented in Sections 3.6 and 3.9 entirely. (2) Asynchronous or jittered multi-fiber recruitment (relaxing the perfectly-synchronous assumption of Section 2.6) would test whether spatial summation requires coincident Aβ firing or tolerates the timing dispersion expected from a real, spatially-extended receptive field. (3) Further refinement of nociceptor channel kinetics, e.g., incorporating Na*v*1.7 (Dib-Hajj et al., 2013) alongside Na*v*1.8/1.9, or adopting a full published parameterization such as Tigerholm *et al.* or Sundt *et al.* (Sundt et al., 2015; Tigerholm et al., 2014) in place of the simplified constant-time-constant formulation used here, could widen the narrow graded-sensitization window identified in Section 3.8. (4) A 3D finite-element EMI representation (Jæger et al., 2021; Jæger & Tveito, 2026) of the true, non-uniform extracellular geometry at a compression or demyelination site, applied to a multi-fiber bundle rather than a single fiber pair, would address the two most consequential simplifications in this study (1D geometry and the explicit-coupling ceiling) simultaneously. (5) Decoupling nodal membrane area from grid resolution (Section 3.1), e.g., by fixing each node of Ranvier's physical width independent of Δz, would remove the discretization-dependence identified in the conduction-velocity convergence check and allow a grid-independent CV to be reported.

6 Conclusion

A closed-loop, biophysically validated core-conductor model coupling a myelinated Aβ-fiber and a C-fiber through a shared, pathologically restricted extracellular space finds no evidence that single-fiber-pair ephaptic crosstalk (under single-pulse stimulation, plausible tonic sensitization, or high-frequency temporal summation) is sufficient to trigger an ectopic nociceptor spike, and this conclusion holds under both classical Hodgkin-Huxley and literature-derived Na*v*1.8/Na*v*1.9 nociceptor channel kinetics. Extending the model to a multi-fiber bundle, in which several synchronously-active Aβ afferents share an extracellular compartment with one C-fiber, produces the first substantial, non-artifactual trend toward threshold identified in this study; verified via a dedicated timing/duration/geometry-independence protocol that also exposes a specific, reproducible numerical-artifact signature relevant to any closed-loop ephaptic model using an explicit coupling scheme. This trend does not cross threshold within the numerically trustworthy range (n ≤ 25 fibers), and we do not claim that it would at larger bundle sizes;

rather, this result reframes the central open question of ephaptic allodynia research from whether single-fiber-pair crosstalk is sufficient (it is not) to whether multi-fiber spatial summation is (plausible, unconfirmed), and it identifies the fully implicit multi-fiber solver needed to answer that question.

Abbreviations

Symbol	Definition
$v_{m,k}$	Transmembrane potential of axon k (Aβ = 1, C = 2)
u_e	Shared extracellular potential
r_e, κ	Extracellular longitudinal resistance per unit length; Poisson regularization constant
w_{cleft}	Extracellular cleft width
ρ_i, ρ_e	Axoplasmic / extracellular resistivity
d_1, d_2	Aβ / C-fiber diameter
$\bar{g}18$, $\bar{g}19$	Maximum Nav1.8 / Nav1.9 conductance density
ΔV_{shift}	Uniform HH gating-kinetics voltage shift (Phase 1 sensitization)
n	Number of synchronously-active Aβ fibers (multi-fiber bundle)
Δz, Δt	Spatial / temporal discretization step

Declarations

Competing Interests

No competing interests to declare that are relevant to the content of this article.

Ethics Approval

Not applicable. This study involves only computational simulation; no human participants, human data, or animal subjects were used.

Funding

No funding was received for this work.

Author Contribution

[M.S.] conceived and designed the study, developed the computational model (the closed-loop core-conductor formulation, the classical Hodgkin-Huxley and Nav1.8/Nav1.9 channel kinetics, and the multi-fiber bundle extension), implemented the simulation software, performed all simulations and analyses, diagnosed and characterized the numerical artifacts reported in the paper, prepared all figures, and wrote the manuscript. [M.S.] read and approved the final manuscript.

Data Availability

The simulation code implementing the core-conductor model, the CRRSS, classical HH, and Nav1.8/Nav1.9 kinetics, the multi-fiber bundle formulation, and the artifact-detection protocols described in this paper is available on this public GitHub repo: https://github.com/MinaSaied23/ephaptic-crosstalk

Code Availability

The simulation code implementing the core-conductor model, the CRRSS, classical HH, and Nav1.8/Nav1.9 kinetics, the multi-fiber bundle formulation, and the artifact-detection protocols described in this paper is available on this public GitHub repo: https://github.com/MinaSaied23/ephaptic-crosstalk please contact me directly on my provided email address for any further questions.

References

1. Akopian, A. N., Sivilotti, L., & Wood, J. N. (1996). A tetrodotoxin-resistant voltage-gated sodium channel expressed by sensory neurons. *Nature*, *379*(6562), 257–262.
2. Amir, R., & Devor, M. (2000). Functional cross-excitation between afferent A- and C-neurons in dorsal root ganglia. *Neuroscience*, *95*(1), 189–195.
3. Arvanitaki, A. (1942). Effects evoked in an axon by the activity of a contiguous one. *Journal of Neurophysiology*, *5*(2), 89–108.
4. Asmedi, A., Wibowo, S., & Meliala, L. (2018). Ephaptic crosstalk in painful diabetic neuropathy: An electrodiagnostic study. *Journal of Medical Sciences (Berkala Ilmu Kedokteran)*, *50*(2), 173–179.
5. Baker, M. D., Chandra, S. Y., Ding, Y., & Waxman, S. G. (2003). GTP-induced tetrodotoxin-resistant Na^+ current regulates excitability in mouse and rat small diameter sensory neurones. *Journal of Physiology*, *548*(2), 373–382.

6. Bokil, H., Laaris, N., Blinder, K., Ennis, M., & Keller, A. (2001). Ephaptic interactions in the mammalian olfactory system. *Journal of Neuroscience*, *21*(20), RC173.
7. Capllonch-Juan, M., & Sepulveda, F. (2020). Modelling the effects of ephaptic coupling on selectivity and response patterns during artificial stimulation of peripheral nerves. *PLOS Computational Biology*, 16(6), e1007826.
8. Chiu, S. Y., Ritchie, J. M., Rogart, R. B., & Stagg, D. (1979). A quantitative description of membrane currents in rabbit myelinated nerve. *Journal of Physiology*, *292*(1), 149–166.
9. Clark, J. W., & Plonsey, R. (1968). The extracellular potential field of the single active nerve fiber in a volume conductor. *Biophysical Journal*, *8*(7), 842–864.
10. Cummins, T. R., Dib-Hajj, S. D., Black, J. A., Akopian, A. N., Wood, J. N., & Waxman, S. G. (1999). A novel persistent tetrodotoxin-resistant sodium current in SNS-null and wild-type small primary sensory neurons. *Journal of Neuroscience*, *19*(24), RC43.
11. Devor, M., & Wall, P. D. (1990). Cross-excitation in dorsal root ganglia of nerve-injured and intact rats. *Journal of Neurophysiology*, *64*(6), 1733–1744.
12. Dib-Hajj, S. D., Yang, Y., Black, J. A., & Waxman, S. G. (2013). The NaV1.7 sodium channel in health and disease. *Nature Reviews Neuroscience*, *14*(1), 49–62.
13. Goldwyn, J. H., & Rinzel, J. (2016). Neuronal coupling by endogenous electric fields: Cable theory and applications to coincidence detector neurons in the auditory brain stem. *Journal of Neurophysiology*, *115*(4), 2033–2051.
14. Han, K. S., Guo, C., Chen, C. H., Witter, L., Osorno, T., & Regehr, W. G. (2018). Ephaptic coupling promotes synchronous firing of cerebellar Purkinje cells. *Neuron*, *100*(3), 564–578.
15. Hodgkin, A. L., & Huxley, A. F. (1952). A quantitative description of membrane current and its application to conduction and excitation in nerve. *Journal of Physiology*, *117*(4), 500–544.
16. Jæger, K. H., Tveito, A., et al. (2021). A cell-based Extracellular-Membrane-Intracellular (EMI) model of excitable tissue. *Frontiers in Physiology*, *12*, 811029.
17. Jæger, K. H., & Tveito, A. (2026). Extracellular stimulation and ephaptic coupling of neurons in a fully coupled finite element-based Extracellular-Membrane-Intracellular (EMI) model. *Frontiers in Computational Neuroscience*, *20*, 1755548.
18. Katz, B., & Schmitt, O. H. (1940). Electric interaction between two adjacent nerve fibres. *Journal of Physiology*, *97*(4), 471–488.
19. Klein, A. H., Vyshnevska, A., Hartke, T. V., De Col, R., Mankowski, J. L., Turnquist, B., Bosmans, F., Reeh, P. W., Schmelz, M., Carr, R. W., & Ringkamp, M. (2017). Sodium channel NaV1.8 underlies TTX-resistant axonal action potential conduction in somatosensory C-fibers of distal cutaneous nerves. *Journal of Neuroscience*, *37*(21), 5204–5214.
20. Lin, J., & Keener, J. (2010). Ephaptic coupling is a mechanism of conduction reserve during reduced gap junction coupling. Proceedings of the National Academy of Sciences, 107(49), 21078–21083.

21. Lindén, H., Hagen, T., Łęski, S., Norheim, E. S., Pettersen, K. H., & Einevoll, G. T. (2014). LFPy: A tool for biophysical simulation of extracellular potentials generated by detailed model neurons. *Frontiers in Neuroinformatics*, *7*, 41.
22. Marshall, D. P., Farah, E. S., Musselman, E. D., Pelot, N. A., & Grill, W. M. (2025). PyFibers: An open-source NEURON-Python package to simulate responses of model nerve fibers to electrical stimulation. *PLOS Computational Biology*, 21(12), e1013764.
23. Pelot, N. A., Catherall, D. C., Thio, B. J., Titus, N. D., Liang, E. D., Henriquez, C. S., & Grill, W. M. (2021). Excitation properties of computational models of unmyelinated peripheral axons. *Journal of Neurophysiology*, *125*(5), 1770–1790.
24. Rappaport, Z. H., & Devor, M. (1994). Trigeminal neuralgia: The role of self-sustaining discharge (ignition) in the medicine and surgery of paroxysmal pain. *Pain*, *56*(2), 127–138.
25. Rasminsky, M. (1980). Ephaptic transmission between single nerve fibres in the spinal nerve roots of dystrophic mice. *Journal of Physiology*, *305*(1), 151–169.
26. Rossoni, E., Tirozzi, B., & McDonald, M. S. (2003). A model of action potential propagation in bundles of myelinated nerve fibers. *Biological Cybernetics*, *89*(6), 430–440.
27. Schlötter, M., Maret, G. U., & Kleineidam, C. J. (2023). Annihilation of action potentials induces electrical coupling between neurons. *eLife*, *12*, RP88335.
28. Schmidt, H., Hahn, G., Deco, G., & Knösche, T. R. (2021). Ephaptic coupling in white matter fibre bundles modulates axonal transmission delays. *PLOS Computational Biology*, 17(2), e1007858.
29. Schmidt, H., & Knösche, T. R. (2022). Modelling the effect of ephaptic coupling on spike propagation in peripheral nerve fibres. *Biological Cybernetics*, *116*(4), 461–473.
30. Seltzer, Z., & Devor, M. (1979). Ephaptic transmission in chronically damaged peripheral nerves. *Neurology*, *29*(7), 1061–1064.
31. Shifman, A. R., & Lewis, J. E. (2019). ELFENN: A generalized platform for modeling ephaptic coupling in spiking neuron models. *Frontiers in Neuroinformatics*, *13*, 35.
32. Sundt, D., Gamper, N., & Jaffe, D. B. (2015). Spike propagation through the dorsal root ganglia in an unmyelinated sensory neuron: A modeling study. *Journal of Neurophysiology*, *114*(6), 3140–3153.
33. Sweeney, J. D., Mortimer, J. T., & Durand, D. M. (1987). Modeling of mammalian myelinated nerve for functional neuromuscular stimulation. In Proceedings of the 9th Annual Conference of the IEEE Engineering in Medicine and Biology Society (pp. 1577–1578).
34. Tigerholm, J., Petersson, M. E., Obreja, O., Lampert, A., Carr, R., Schmelz, M., & Fransén, E. (2014). Modeling activity-dependent changes of axonal spike conduction in primary afferent C-nociceptors. *Journal of Neurophysiology*, *111*(8), 1721–1735.
35. Veeraraghavan, R., Lin, J., Hoeker, G. S., Keener, J. P., Gourdie, R. G., & Poelzing, S. (2015). Sodium channels in the Cx43 gap junction perinexus may constitute a cardiac ephapse: An experimental and modeling study. *Pflügers Archiv - European Journal of Physiology*, *467*(10), 2081–2093.

Figures

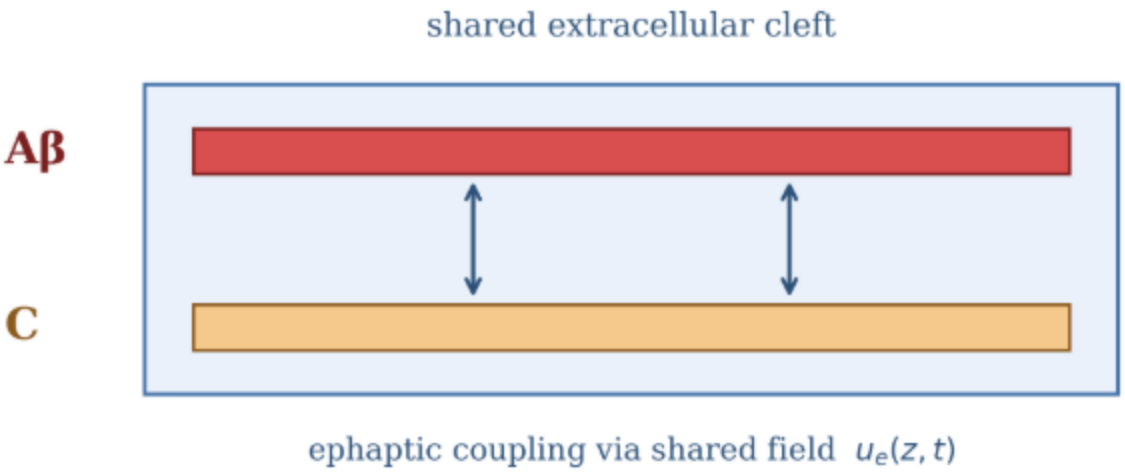


Figure 1

Model architecture (simplified schematic). A myelinated Aβ fiber and an unmyelinated C-fiber are embedded in a shared, geometrically restricted extracellular cleft. Both fibers' transmembrane ionic currents drive a regularized Poisson equation for the shared extracellular potential u_e(z,t), which is solved at every integration time step and fed back into each fiber's cable equation as an ephaptic driving term (double-headed arrows), closing the loop. Full biophysical detail (nodes of Ranvier, internodal myelin, the governing equations, and the multi-fiber extension) is given in Section 2

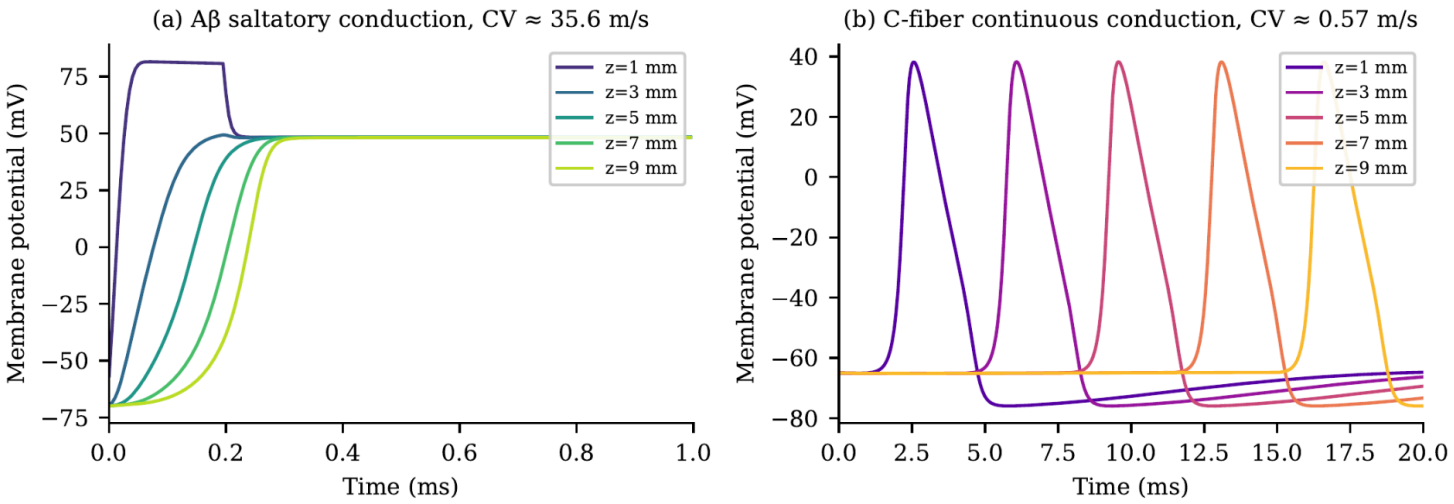


Figure 2

Positive control confirming both Phase 1 fiber models are independently excitable and conduct correctly, with ephaptic coupling disabled. (a) Isolated Aβ-fiber: saltatory action potential recorded at five nodes of Ranvier (z = 1–9 mm) following a 100 nA, 0.2 ms current pulse at z = 0, propagating at ≈35.6 m/s. (b) Isolated classical-HH C-fiber: continuously conducted action potential recorded at five positions (z = 1–9 mm) following a 1 nA, 1 ms current pulse at z = 0, propagating at ≈0.57 m/s. Both fibers reach full

regenerative spike amplitude at every recorded location, confirming that the negative results of Sections 3.2–3.6 reflect insufficient ephaptic drive rather than an intrinsically inexcitable C-fiber model

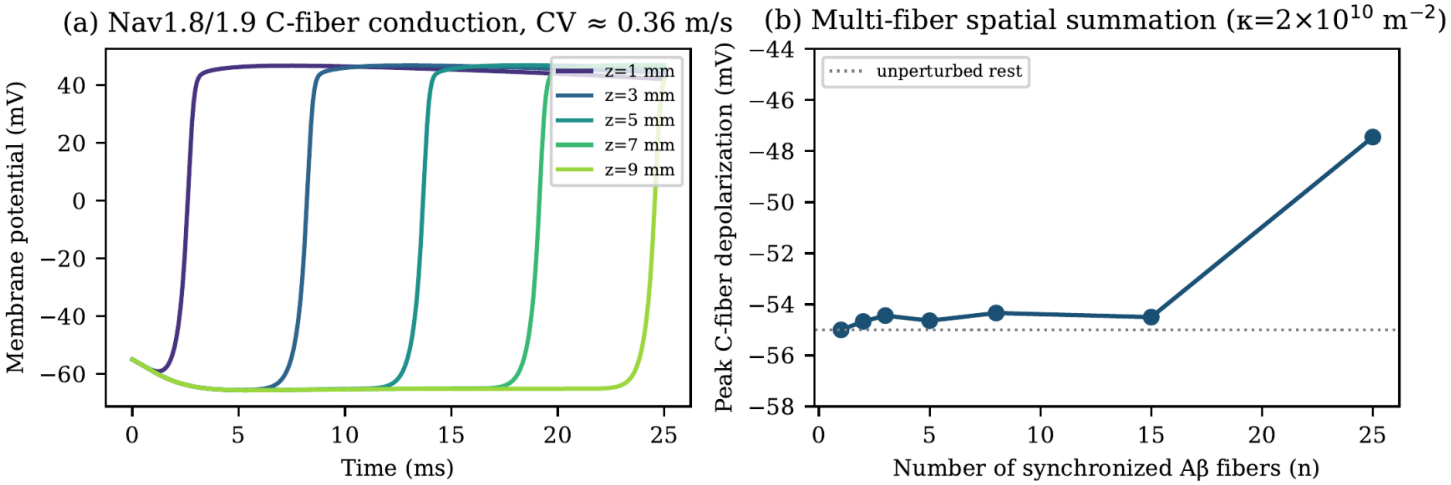


Figure 3

(a) Positive control for the Phase 2 C-fiber: isolated Nav1.8/1.9 C-fiber conducting continuously at ≈0.36 m/s (z = 1–9 mm, 3 nA/1 ms stimulus at z = 0), confirming the nociceptor-realistic channel model is independently excitable and propagating before closed-loop coupling is introduced. (b) Multi-fiber spatial summation trend (Section 3.9): peak C-fiber depolarization vs. number of synchronized Aβ fibers n, at κ = 2×10^{10} m^{-2}, restricted to the range (n ≤ 25) independently verified stable under extended-duration simulation. The monotonic ≈8 mV trend does not cross threshold within this verified range